

Measuring Nano to Micro Structures from Relayed DNP NMR

Arthur C. Pinon,¹ Judith Schlagnitweit,^{2,4} Pierrick Berruyer,⁴ Aaron J. Rossini,^{1,5} Moreno Lelli,⁶ Etienne Socie,¹ Mingue Xue Tang,⁷ Tran Pham,³ Anne Lesage,⁴ Staffan Schantz,⁸ and Lyndon Emsley.¹

¹Institut des Sciences et Ingénierie Chimiques, Ecole Polytechnique Fédérale de Lausanne (EPFL), CH-1015 Lausanne, Switzerland.

²Karolinska Institutet, Stockholm, Sweden

³GSK Medicines Research Centre, Stevenage, SG1-2NY, United Kingdom.

⁴Centre de Résonance Magnétique Nucléaire (RMN) à Très Hauts Champs, Institut des Sciences Analytiques (CNRS/ENS de Lyon/UCB Lyon 1), Université de Lyon, 69100 Villeurbanne, France.

⁵Department of Chemistry, Iowa State University, Ames, IA 50011-3111, USA.

⁶Department of Chemistry, University of Florence, Center for Magnetic Resonance, 50019 Sesto Fiorentino (FI), Italy

⁷National High Magnetic Field Laboratory, 1800 East Paul Dirac Drive, Tallahassee, FL-32310, USA.

⁸Pharmaceutical Development, AstraZeneca R&D Mölndal, SE-431 83 Mölndal, Sweden

ABSTRACT: We show how DNP NMR can be used in combination with models for polarization dynamics to determine the domain sizes in complex materials. By selectively doping a source component with radicals, and leaving the target undoped, we can measure experimental polarization build-up curves which can be compared with simulations based on heterogeneous distributions of polarization within the sample. The variation of the integrated DNP enhancement as a function of the polarization time is found to be characteristic of the geometry. We demonstrate the method experimentally on four different systems where we successfully determine domain sizes between 200 and 20 000 nanometers, specifically in: powdered histidine hydrochloride monohydrate, pore lengths of mesoporous silica materials, and two domain sizes in two-component polymer film coatings. Additionally, we find that even in the apparently homogeneous frozen solutions used as polarization sources in most DNP experiments, polarization is relayed from protons near the radicals to the bulk of the solution by spin diffusion, which explains the experimentally observed build-up times in these samples.

INTRODUCTION

Modern materials such as polymers or pharmaceuticals, as well as porous materials, are usually well-designed nano- or micro structured (multicomponent) systems. The physical properties of these materials are strongly related to particle sizes, pore sizes or pore lengths, and domain sizes. Therefore, methods to determine architectures on these nano- to micrometer length scales are necessary for the development of next generation materials.

Depending on the nature of the sample, domain sizes may be measurable by laser diffraction, scattering methods, or by electron microscopy methods.¹⁻³ However, in complex multicomponent mixtures, these methods become much more difficult to apply. NMR would be a method of choice in these cases. Indeed, based on chemical shift differences or relaxation properties of different compounds, NMR often allows clear distinction among components. Consequently, the study of *in situ* domain sizes becomes feasible with NMR methods.

Proton spin diffusion experiments are the most widely used methods for domain size measurement.^{4,5} In these experiment an initial spatially heterogeneous non-equilibrium distribution of magnetization is created, and the return to equilibrium driven by spin diffusion is monitored.⁶ In order to create the non-equilibrium distribution by selecting proton magnetization from particular domains, different procedures have been proposed including filters based on dipolar couplings,^{5,7,8} differences in relaxation properties,⁶ or proton or carbon chemical shift differences.⁹⁻¹³ These methods work well in two-

component systems where the components exhibit significant differences in the properties chosen for selection. However, for more complex multiple component systems these methods are usually not feasible.

It has recently been shown that domain sizes can be determined in complex systems using dynamic nuclear polarization (DNP) where the non-equilibrium distribution of magnetization is obtained by locally enhancing polarization.¹⁴⁻¹⁷ It has also been shown that the selection process can be replaced by selective doping of one of the domains of the diamagnetic system with paramagnetic species, and using paramagnetic relaxation enhancement to estimate the domain sizes.¹⁸

In these approaches, the initial out of equilibrium state is achieved by selective doping followed by either comparison with spin diffusion dynamics in an undoped sample, or comparison to a state in which the doped region is hyperpolarized. The curves obtained through comparison of the two initial states for different recovery times in saturation-recovery experiments can then be interpreted using numerical solutions of the diffusion equations.

The DNP method has previously been used to determine domain sizes for an active pharmaceutical ingredient (API), cetirizine dihydrochloride, in a drug formulation.¹⁷ Griffin and coworkers previously studied the diffusion of polarization through peptide nanocrystals in a frozen solution.¹⁴

Here we present a general approach to model the relay of hyperpolarization in these experiments, and we provide a detailed analysis of four different archetypal geometries. Experimental validation is given with the determination of particle sizes in powdered histidine hydrochloride monohydrate, the pore lengths of mesoporous silica materials, and two domain sizes in two-component polymer film coatings. We show that with typical values of the relaxation and diffusion rates in organic solids, the method is sensitive to architectures with sizes from 50 nm to 20 μm . We also provide analytical approximations that allow us to relate steady-state DNP enhancements values to the micro-architecture of the systems. In particular, we find that the analysis is also applicable to the nanoscale heterogeneity in the bulk polarizing solution itself.

EXPERIMENTAL

Sample Preparation

Powdered histidine hydrochloride monohydrate was obtained from Sigma Aldrich and used without further purification. For DNP enhanced NMR experiments on powdered histidine hydrochloride monohydrate, the organic powder was either used as is, or was finely ground by hand in an agate mortar and pestle for several minutes. Incipient wetness impregnation (IWI)¹⁹ was used to uniformly wet the surface of around 30 mg of the powdered solid with around 15 μL of a solution containing 16 mM of the state of the art biradical polarizing agent TEKPol in 1,1,2,2-tetrachloroethane (TCE).²⁰ Alternatively, a few milligrams of powder was dissolved in a solution containing 12 mM of the biradical AMUPol in glycerol- d_8 :D₂O:H₂O (6:3:1) to obtain a homogeneous mixture.²¹ Samples were then transferred to a sapphire rotor, packed with a polytetrafluoroethylene (PTFE) insert, and capped with a PTFE or vespel cap.

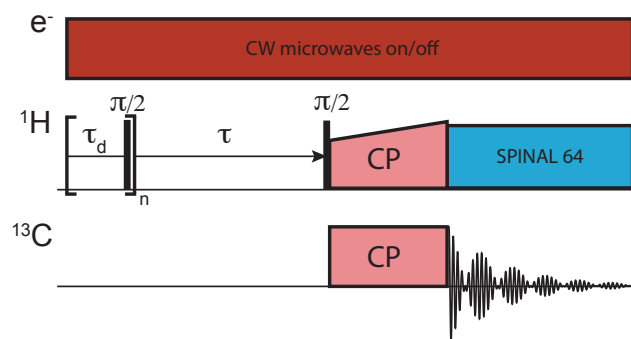
The mesoporous materials were synthesized as described in SI. For DNP enhanced NMR experiments on passivated mesoporous SBA-15 functionalized with a propylimidazolium group, between 30 to 40 mg of the silica-based mesoporous material was wetted with between 10 to 20 μL of a solution containing 16 mM of the binitroxide polarizing agent TEKPol2 in 1,1,2,2-tetrachloroethane solution.²²

Coated pellet samples, consisting of a microcrystalline cellulose (MCC) core, spray coated with a film of ethyl cellulose (EC) and hydroxypropyl cellulose (HPC) in a ratio of 70/30 were provided by AstraZeneca. For DNP enhanced NMR experiments about 15 μL of 16 mM biradical solution TOTAPOL in glycerol- d_8 :D₂O:H₂O (6:3:1) were added to about 30 mg of pellets. The wet sample was then mixed with a glass stirring rod and transferred to a sapphire rotor, packed with a PTFE insert, and capped with a PTFE cap.

DNP Enhanced NMR Spectroscopy

DNP enhanced solid-state NMR experiments were performed on wide bore 400 MHz ($B_0 = 9.4$ T) Bruker Avance I and Avance IIIHD spectrometers both equipped with 263 GHz gyrotrons, a low temperature cooling cabinet, and a triple resonance 3.2 mm low temperature magic angle spinning (MAS) probe. The sample temperature for DNP experiments was approximately 105 K. The sweep coil of the main magnetic field ($\nu_0(^1\text{H}) = 400.432$ MHz) was set so that microwave irradiation occurred at the same position as the ϵ maximum for TOTAPOL.²³ The estimated power of the microwave beam at the output of the waveguide was approximately 4 to 8 W. The sample spinning rate (ν_{rot}) was 8000 Hz. For all CP experiments the amplitude of the ^1H RF field was ramped during the contact time to improve efficiency.²⁴

Low temperature solid-state NMR experiments without DNP were performed on a wide bore 500 MHz (i.e., $B_0 = 11.74$ T) Bruker III HD spectrometer equipped with a low temperature cooling cabinet, and a triple resonance 3.2 mm low temperature magic angle spinning (MAS) probe. The sample temperature was approximately 105 K.



Scheme 1. The saturation-recovery ^1H - ^{13}C CP pulse sequence used for acquisition of spectra. τ_d was set to 20 ms, and n to 20. τ is the polarization delay.

Numerical Simulations

Numerical simulations were performed using the Matlab differential equation solver “pdepe”, which solves initial-boundary condition problems for partial differential equations in space (x) and time (t) domains. Two different differential equations were used for the cases where the microwave irradiation (μwave) is on or off. Initial and boundary conditions do not change between the μwave on and off cases, whereas the local equilibrium polarization P_0 changes between μwaves on ($P_{0,\text{on}}$) and μwaves off ($P_{0,\text{off}}$) cases. The values of T_1 or T_B , and P_0 were defined using the hyperbolic secant functions described in the main text and in SI. Both for μwaves on and off cases, numerical values of the polarization function that satisfy the differential equations were found and the polarization was scaled by $|J(x)|$ where $|J(x)|$ is the Jacobian as described in the results section. The simulated signal was obtained by integration of the resulting polarization using a trapezoidal numerical integration. The simulated enhancement was calculated as the ratio of the integrated μwaves on and off signals. The normalization factors for the signals were obtained using the value of the signal at steady state. The Matlab code is available with the SI. Automatic fits were performed with Matlab using the least squares method for both the enhancement and the build-up data.

RESULTS AND DISCUSSION

Spin Diffusion Related DNP.

The basic principle behind the idea of measuring domain structures with DNP or PRE experiments is that the sample can be prepared in a way that one component contains a polarization agent, and will be referred to here as the source, while a second component is free of polarizing agents, and will be referred to as the target. When the source is hyperpolarized, polarization builds up quickly, and then diffuses into the target through homo-nuclear proton spin-diffusion. The build-up of the polarization in the target thus depends on its size.

The observable build-up time of a compound resonance subject to spin diffusion in a saturation-recovery experiment can be quite different from the “intrinsic” build-up time. This effective build-up time has been previously referred to as T_B ,²⁵ T_1 ,²⁶ T_1^{*18} or T_{DNP}^{27} . Here it is essential to differentiate the intrinsic build-up time from both the μwaves on and μwaves off effective build-up times, the following notation will be used:

T_1 is the ^1H relaxation time measured during a saturation-recovery experiment on a pure dry solid.

T_B is the effective ^1H build-up time measured when the sample is doped with paramagnetic species; $T_{B,\text{OFF}}$ in the absence of μwave irradiations, and $T_{B,\text{ON}}$ in the presence of μwave irradiations.

In order to determine sizes quantitatively, we must develop a numerical model for the process, as described in the following.

The model used to describe the saturation-recovery experiments investigated here is based on a system containing at least two distinct domains. The source is selectively doped with a paramagnetic species, while the target remains undoped. The source also undergoes paramagnetic relaxation enhancement (PRE) induced by the presence of radicals.²⁸ We assume that the border between the two domains has a finite width, and we describe this interfacial region by a gradient function moving from pure source to pure target.

In the following, we model a system in which the recovery towards equilibrium for the two different components will not be a single mono-exponential function with $T_{1,\text{source}}$ and $T_{1,\text{target}}$. Rather, multi exponential build-up will be observed for both components if the domain sizes of the source and target are comparable to the distances over which spin diffusion can transport polarization on the T_1 time-scales. We define the characteristic diffusion length as $\rho = \frac{x}{\sqrt{DT_1}}$ (see details in SI). If the domain sizes are very small compared to the characteristic diffusion length, $\rho \ll 1$, $L \ll \sqrt{\langle D \rangle \langle T_1 \rangle}$, then both components will appear to relax towards equilibrium with the same build-up time, T_b . If the domain sizes are very large, $L \gg \sqrt{\langle D \rangle \langle T_1 \rangle}$ compared to the diffusion length, then both components will appear to relax towards equilibrium with their intrinsic build-up times $T_{1,\text{source}}$ and $T_{1,\text{target}}$. In the intermediate regime, where the domain sizes are comparable to the diffusion length, relaxation towards equilibrium will appear multi-exponential, and will be a function of the size and geometry of the domains. It is this effect that we exploit here. This basic principle of spin diffusion relayed relaxation has been introduced and used widely in the past in both solids and solutions.^{14-18,26,29-38} One of the particularities here is that we introduce differential relaxation into a normally diamagnetic sample by selective doping of one domain, and that we can then determine geometries by comparing polarization dynamics in experiments that are otherwise identical except for the initial conditions of the value of T_1 in the dopant (which corresponds to relayed-PRE¹⁸) or, here, by changing the equilibrium polarization of the dopant with DNP.

We also remark that recently there has been considerable interest in developing computational models for spin diffusion^{39-43,44} and for different aspects of spin dynamics specifically in DNP experiments^{43,45}. Some very interesting work has been done to include the role of the depolarization induced by the biradicals under the MAS rotation.^{46,47} However, since we are concerned here with length scales beyond ~ 50 Å we adopt a method that is based solely on transport by spin diffusion.^{14,15}

Numerical Models for Spin Diffusion Relayed DNP.

The polarization dynamics is described by the following differential equation, where we assume the transfer of polarization behaves like thermal or other classical diffusion processes that follows Fick's second law:^{6,48,49}

$$\frac{\partial P(x, t)}{\partial t} = D(x) \cdot \Delta P - \frac{P(x, t) - P_0(x)}{T_1(x)} \quad (1)$$

where x is the position vector distance from the border between source and target in μm , t is the time in seconds ($0 < t < \infty$), P is the instantaneous polarization (arbitrary units), P_0 is the local equilibrium polarization, D is the diffusion rate at position x , T_1 is the longitudinal relaxation time at position x , and ΔP is the Laplacian of the polarization whose formal expression depends on the symmetry of the system (see details in SI).

In practice, depending on the nature of the physical interface between the source and the target, the thickness of the border will vary, as discussed later in the text. We consider two different functions for

the change in NMR parameters at the interface. The first is the case for an interface that is a step function, and where the NMR properties then change as $1/r^6$ beyond the interface (function described in details in SI). The second would be appropriate when the interface itself extends over a range of distance, and where we consider that the gradient between the components at the crossover follows (for example) a hyperbolic tangent function, as shown in Figure 1. When the border is only 2 nm thick, the $1/r^6$ dependence is most appropriate, but the shape of the function has little or no effect on the observables since the objects considered here are on the order of μm wide. For objects for which the border is significantly thicker, the hyperbolic secant is more appropriate to describe a gradient of radicals. For the sake of convenience, we chose to use here the hyperbolic secant function to describe the transition at the interface. However, as required, different functions could be used for the three variables, that might more accurately reproduce the physical and spatial dependencies of the interactions. The hyperbolic secant functions are described in detail in SI.

Equation (1) does not have a general analytical solution. Under certain approximations, we can find some general analytical solutions as described in SI. Here, we resort to numerical solutions with the following boundary conditions:

$$P(x, 0) = 0 \quad (2)$$

$$\left(\frac{\partial P(x, t)}{\partial x} \right)_{x_0} = 0 \quad (3)$$

where x_0 corresponds to the position at the extremity of the system. The first condition corresponds to no initial polarization inside the system (for saturation-recovery experiments), and the second corresponds to the absence of polarization flux at the edge of the system. The second condition implies no flux of polarization at the center of the target nor at the edge of the source. Notably we model the entire system as a single continuous object, and we do not need to partition the system (as long as the numerical solutions converge).

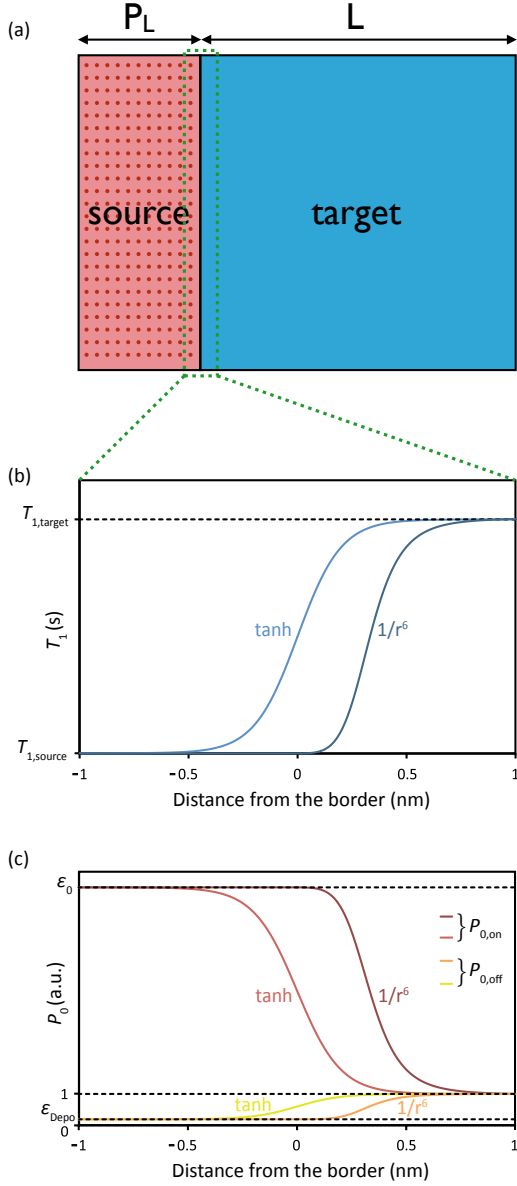


Figure 1. (a) Schematic representation of a system containing a source and a target. The source has a length P_L and is doped with e.g. organic radicals, whereas the target has a length L and remains undoped. Red dots represent schematically the presence of radicals. Hyperbolic tangent (\tanh) and $1/r^6$ functions describe in (b) the relaxation time T_1 and in (c) the local equilibrium polarization P_0 as a function of the distance from the border.

Small targets and homogeneous bulk solutions.

As shown in Figure 2a, a solution containing dissolved radicals can already be described using this general formalism. In this case the average distance between sources (where each radical molecule act as a polarization source) is short enough that spin diffusion equalizes the polarization throughout the sample on a timescale short compared to the characteristic build-up times. This case corresponds to the situation of a bulk polarizing solution, e.g. containing a biradical such as TEKPol or AMUPol.

In this case, the average distance between (bi)radicals is defined as twice the Wigner-Seitz radius:⁵⁰

$$\bar{d} = 2\lambda = 2 \left(\frac{3}{4\pi C N_A} \right)^{1/3} \quad (4)$$

where C is the concentration of DNP active radicals, and N_A is Avogadro's number. For a 16 mM solution of biradical, if we assume all the radicals are DNP active for the sake of simplicity (though some fraction is probably not active, which would lead to a lower concentration of sources than relaxation sinks), we find a distance of 5.8 nm. With a diffusion constant of $10^{-4} \mu\text{m}^2\text{s}^{-1}$, the volume between two radicals is polarized by spin diffusion in less than 10 ms. This quasi-instantaneous spin diffusion leads to the observation of a mono exponential build-up for a bulk solution of radicals, despite the fact that the source and target areas have different intrinsic T_1 . However, very importantly, a significant part of the solvent is mostly polarized by relayed transfer, and therefore the concentration of radicals does influence the observed DNP build-up time of the system. This has also been postulated very recently in simulations by Mentink-Vigier *et al.*⁴⁵

As illustrated in Figure 2a, we define a volume close to the radical, V_Q , in which ^1H spins undergo strong paramagnetic interaction because of the hyperfine coupling between nuclear and electron spins which leads to, for example, large anisotropic shifts or enhanced relaxation and quenching of the nuclear polarization. The large shift anisotropy makes that spins inside V_Q communicate each other much less efficiently, and that the nuclear spin diffusion is reduced (as an illustrative example, D might decrease from values around $10^{-4} \mu\text{m}^2\text{s}^{-1}$ at the border between V_Q and V_P to about $0 \mu\text{m}^2\text{s}^{-1}$ at the location of the electron, see SI). Additionally, we assume that spins inside V_Q do not produce any observable signal, because of relaxation but also because of the large anisotropic interaction that spread the resonances over a wide spectral windows. We then define a volume, V_P , in which ^1H spins are considered to be directly polarized by the radicals. Finally, as shown in Figure 2a, the remaining volume, V_{SD} , is not directly polarized by the radicals. In this model the spins inside both V_P and V_{SD} are observable, and they are in contact by spin diffusion. Thus, in relation to Figure 1, $V_P + V_Q$ constitute the source, and V_{SD} is the target. The intrinsic T_{1,V_P} and T_{1,V_Q} of spins contained in V_P and V_Q are not directly measurable since we do not know *a priori* the ratio between V_P , V_Q and V_{SD} in a given sample.

In Figure 2, to determine T_{1,V_P} and T_{1,V_Q} , we measure the build-up time T_B of a series of samples without μ wave irradiations and with different radical concentrations, for TEKPol in TCE at 105 K. The data are then fit using the numerical model described above. The best fit between simulated and experimental build-up times was found for $V_Q = V_P = 3.8 \pm 0.1 \text{ \AA}$, $T_{1,V_Q} = 50 \pm 10 \text{ ms}$, $T_{1,V_P} = 80 \pm 10 \text{ ms}$, as shown in Figure 2b. We note that an analogous model was tested, for which the diffusion rate was constant throughout the system ($D = 10^{-4} \mu\text{m}^2\text{s}^{-1}$) which gave slightly worse fits with only slightly different T_1 s (see SI).

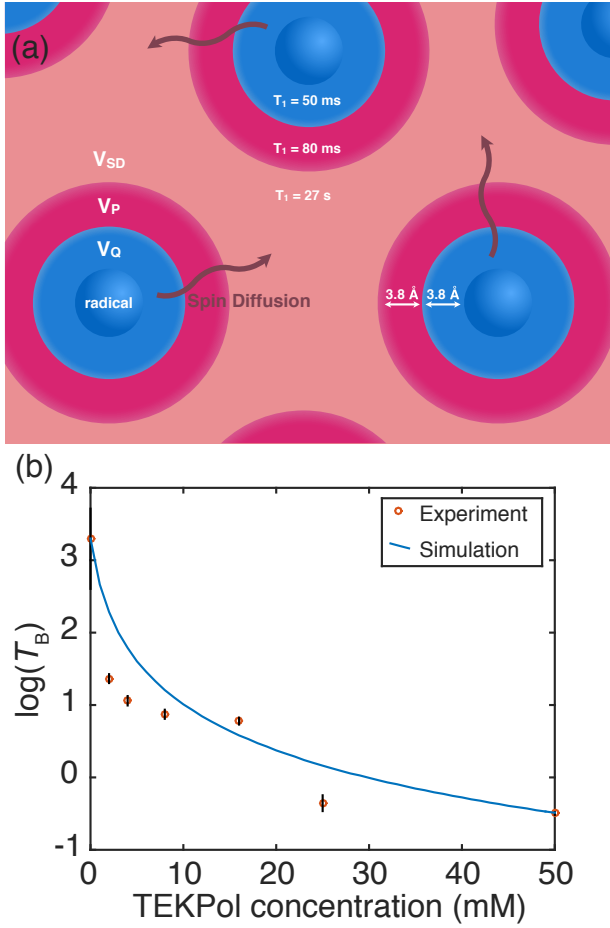


Figure 2. (a) Schematic representation of a bulk radical solution (small target) system. The different components are described in the main text. (b) Experimental ^1H build-up time T_B as a function of the concentration of TEKPol in a frozen solution of TCE at 105 K, with 8 kHz sample spinning recorded on a 500 MHz spectrometer, using saturation-recovery and determined using a mono exponential fit. All samples were degassed using 5 insert-eject cycles prior to measurement to minimize additional paramagnetic relaxation due to dissolved oxygen.⁵¹ The solid blue line is the result of a numerical simulation for a source and target according to (a) for which at each concentration the build-up was simulated and then fit to a mono exponential. In the simulations, the system was assumed to be three-dimensional. $T_{1,VSD}$ was measured to be 27 s (in pure TCE). The size of the volumes V_Q and V_P were determined by fitting to be both $3.8 \pm 0.1 \text{ \AA}$. $T_{1,VQ}$ and $T_{1,VP}$ were determined by fitting to be 50 ± 10 ms and 80 ± 10 ms respectively.

The overall observed build-up time in the polarizing solution varies as a function of concentration because the volume V_{SD} , which has the intrinsic build-up time of the pure solvent (here $T_{1,VSD}$ for pure TCE is measured to be 27 s at 500 MHz), increases as the radical concentration decreases. Since spin diffusion over this length scale is much faster than $T_{1,VSD}$, we therefore observe a single mono exponential build-up time for the sample which is simply a volume weighted average of the three intrinsic build-up times (here $T_{1,VSD} = 27$ s, $T_{1,VP} = 80$ ms and $T_{1,VQ} = 50$ ms) and this explains the typically observable the signal build-up time constants of about 2-3 s typically observed in bulk solutions of 16 mM bi-radicals at around 105 K.^{20-22,52,53} The dependence of the experimental build-up time on residual volume was previously pointed out by Lange *et al.*⁵⁴ in the context of the evaluation of quenching factors.

Large targets and heterogeneous mixtures.

We now move on to consider systems in which the dimension of the target $L \approx \sqrt{\langle D \rangle \langle T_1 \rangle}$. In this case the polarization dynamics will be characteristic of the length and the geometry of the source and the target. In the following we show how to predict these dynamics numerically using Equations (1-3). To do this we need to specify the spatial dependence of T_1 , the local equilibrium polarizations, the diffusion constant, and the effect of depolarization.

Note that, since we will now study the diffusion of polarization on a scale much larger than in the “small targets” section above, we will now refer to the radical+solvent solution as a single source, without considering the V_P or V_{SD} volumes further. Since the source is now a mixture of radicals and solvent, its effective build-up time, which depends on the concentration of radicals, will be referred to as $T_{B,source}$.

The spatial dependence of T_1 as it changes from the source to the target has been described above, and is shown in Figure 1 for r^{-6} and hyperbolic tangent functions. As before, the presence of radicals in the system will induce some signal quenching and/or depolarization in the source.^{19,47} Notably, for cross-effect bi-radicals, depolarization occurs in the source and this will lead to a decrease in the source signal, typically around a factor 0.5 at 8 kHz spinning rate at 9.4 T and 105 K.^{46,47} We remark that depolarization does not play a role in the simulated build-up time for the small target regime described above, but it will influence the behavior in large targets.

The local equilibrium polarization (P_0) is the polarization that each voxel would reach at infinite time if no spin-diffusion occurs. In the absence of microwaves, polarization will tend to recover in the target towards the Boltzmann polarization which we take to be $P_{0,off} = 1$. In the source, however, depolarization may occur in the case of a bi-radical under MAS at rate ν , and the polarization tends to a lower value of the local equilibrium polarization $P_{0,off}(\nu) = \epsilon_{Depo}(\nu)$, where:

$$\epsilon_{Depo}(\nu) = \frac{P_{0,off}(\nu > 0)}{P_{0,off}(\nu = 0)} \quad (4)$$

where $P_{0,off}(\nu > 0)$ and $P_{0,off}(\nu = 0)$ are the μ waves off local equilibrium polarizations of the source for spinning and static samples respectively. In the simulations, we will always take $\epsilon_{Depo} = 0.5$ in line with values found in the literature.⁴⁷

In the presence of μ waves, the local equilibrium polarization within the source is greatly increased, such that $P_{0,on} = \epsilon_0 P_{0,off}$ where ϵ_0 is the DNP enhancement factor of the source in the absence of spin diffusion.

We now note that the steady state source polarization does not necessarily reach the local equilibrium polarization in the presence of spin diffusion from the source to the target. For example, the source polarization close to the interface is higher than the local equilibrium polarization in the absence of μ waves since polarization will diffuse from the target to the interface to compensate MAS driven depolarization. On the other hand, diffusion from the source to the target in the presence of μ waves prevents the source from reaching its equilibrium value. With the typical sizes and diffusion coefficients that we consider here, where the sizes of the source are much larger than the diffusion length, for simplicity we will consider the polarization to be equal to the local equilibrium polarization throughout the source. Thus, the depolarization coefficient defined by Vega and co-workers⁴⁶ as the ratio of signals is quite close that defined as the ratio of polarizations (more details in S1).

Within the target, the equilibrium polarization will decay rapidly to $P_{0,on} = 1$ as the direct DNP effect drops off according to Figure 1, and we choose to model this for simplicity with the same hyperbolic tangent function as used for the changes in T_1 (Figure 1c).

The value of the spin diffusion coefficient D may vary from the source to the target as the proton concentration changes. Since the diffusion coefficient is thought to vary with λ^{-4} where λ is the Wigner-Seitz radius between protons, we then chose to scale the diffusion coefficient with $C^{4/3}$ where C is the ^1H concentration.^{14,16} Moreover, depending on if the sample is amorphous or crystalline and on the temperature, the diffusion rate may vary.

The thickness of the domains also affects spin diffusion dynamics. Indeed, the reservoir of polarization in both domains is not infinite, and for example if there is only a thin layer of source compared to the size of the target this would lead to a depletion of the source under μ wave irradiations, and less hyperpolarization of the target. The source polarization then does not reach $\epsilon_0 P_{0,\text{off}}$. Analogously, in absence of μ waves, a thin source compared to the size of the target would lead to an increase in the source polarization, and the polarization in the source will not reach the $P_{0,\text{off}}(\nu) = \epsilon_{\text{Dopo}}(\nu)$ level, as it would for an undoped sample. These limiting cases may be of interest in certain cases, and particularly for applications in dissolution DNP,⁵⁵ but we will not consider them further here, where we look at cases where the source is always much larger than the diffusion length.

In the following we present examples of polarization dynamics characteristic of different target geometries.

Polarization Dynamics for Different Architectures.

Figure 3 shows the three different archetypal geometries that will be considered and compared to experimental measurements.

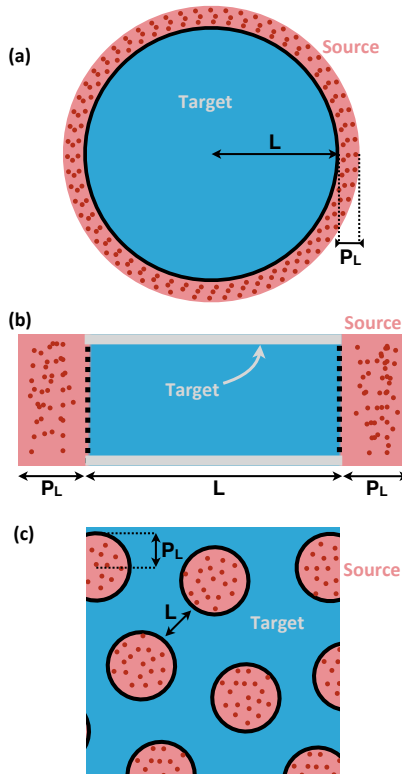


Figure 3. Schematic representation of (a) a spherical organic microcrystal coated with a radical containing solution, (b) a cylinder of pure solvent of length L , which is polarized by radical solution at the ends of the cylinder (this model corresponds for example to a solvent filling the pores in a mesoporous material, and where the radical does not enter the pores), and (c) an organic film containing hydrophilic domains (pink) that are doped with radicals and hydrophobic domains (blue) that remain undoped. Red dots indicate schematically

the presence of radical molecules. In cases (a) and (c), the radical is separated from the target because they are two different compounds: a solid line separates the two domains. In case (b) the target can be either atoms on the wall of the pore or the proton atoms of the pure solvent inside the pore: a dashed line separates the pure solvent (blue) from the radical containing solvent (pink).

The formalisms developed here can be adapted to any geometry, and they are applicable to both DNP and PRE experiments. The three examples we use are chosen since they correspond to common systems of experimental interest. The first system considered is a prototypical organic microcrystal or micro particle. The particle is assumed to be spherical (Figure 3a), and hyperpolarization diffuses into the particle from a layer of impregnating solvent. This corresponds to the situation for ordinary organic powders obtained by grinding and impregnation with a radical containing non-solvent solution,^{15,17} or for a frozen suspension of particles.¹⁴

The second system is considered to be a prototypical pore, which we model as a cylinder (Figure 3b) into which the polarization diffuses from the outside. Since polarization has no known associated viscosity, we assume the diffusion of polarization to be constant over the sample. This model corresponds for example to a solvent filling the pores in a mesoporous material, and where the radical does not enter the pores.^{56,57} The solvent is pure inside the pore, and doped with radical outside the pore.

The third system is prototypical mixture of polymers, where a soluble polymer domain is doped with radical, and insoluble domains remain radical free (Figure 3c).¹⁸ We model this as a one-dimensional network.

Apart from the different symmetries of these geometries, the main difference between them will be the typical sizes and the relative thickness of the border between the source and the target. For example, in the cases of Figure 3a and 3c, the source and the target are two distinct compounds, and the border is well defined. Whereas in the Figure 3b, the transition from doped to undoped solvent is probably more gradual.^{56,57}

The influence of the simulation parameters on the μ wave on polarization and on the enhancement are described in the SI. We use two types of border: one thin (2 nm) and one thick (200 nm). The border defines the area (or volume) in which the parameters described above transition. For both thick and thin border systems, the polarization is propagated numerically through the target until the steady state is reached. The resulting spatial evolution of the polarization as a function time for a spherically symmetric system is plotted in Figure 4.

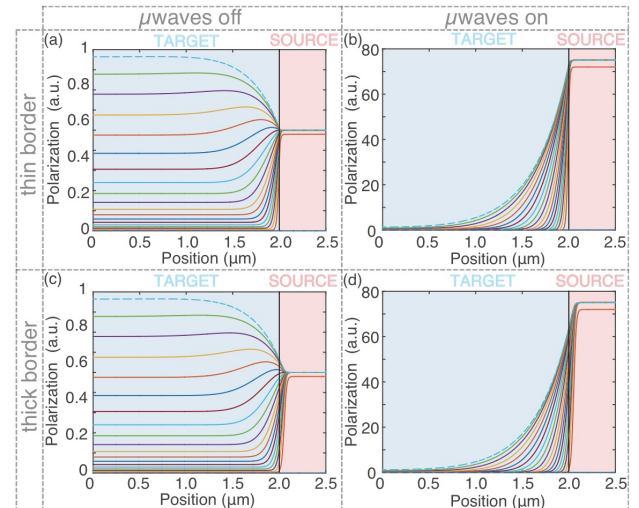


Figure 4. Simulations of polarization as a function of the position for a spherically symmetric system (a) & (c) in absence and (b) & (d) presence of microwave irradiation, for different times from $t = 0$ to 200 s (where a steady state is reached, dashed light blue lines) with exponential time increment. (a) & (b) have a thin border (2 nm) whereas (c) & (d) have a thick border (200 nm). The source is shown in red, whereas the target is shown in blue. In both cases, $L = 2 \mu\text{m}$, $T_{B,\text{source}} = 100 \text{ ms}$, $T_{1,\text{target}} = 100 \text{ s}$, $\epsilon_{\text{Depo}} = 0.5$, $\epsilon_0 = 150$, $D_{\text{target}} = D_{\text{source}} = 1.0 \cdot 10^{-3} \mu\text{m}^2 \text{ s}^{-1}$, and $P_L = 0.5 \mu\text{m}$.

The polarization is then integrated over the desired region, giving a signal:

$$S_{\text{on/off}}(t) = \frac{1}{V} \int_V P_{\text{on/off}}(x, t) \cdot |J(x)| \cdot dx \quad (6)$$

where S_{on} and S_{off} correspond respectively to the signals with and without microwave irradiation, P_{on} and P_{off} correspond to the polarization with and without microwaves irradiation, and $|J(x)|$ corresponds to the Jacobian determinant: $|J(x)| = 1$ for linear symmetry, and for spherical symmetry, after integration on the angular coordinates, we have $|J(x)| = 4\pi x^2$. (The adaptation to other geometries can be done, for example, for a system where spin diffusion can occur in two dimensions: the Jacobian thus has to be equal to $2\pi x$. Other changes also have to be made in the diffusion equation (1), as described at the end of the results section.)

Archetypal signal build-up curves for the target for μwave on and off are plotted in Figures 5a for the thin and thick border cases. We immediately note that the recovery is accelerated in the presence of μwaves , and this is the primary signature of relayed DNP.

We then note that the main difference between the thin and thick border cases occurs at early times. This is not surprising, since at early times the target hyperpolarization is located at the border between the source and the target. Its thickness then determines the intensity of the signal at early times.

The enhancement as a function of time can be then trivially calculated:

$$\varepsilon(t) = \frac{S_{\text{on}}(t)}{S_{\text{off}}(t)} \quad (7)$$

Figure 5b shows enhancement versus time for the same cases. We remark that the enhancement varies significantly with time, and this is a key signature of heterogeneous polarization, and relayed transfer. Indeed, if the sample polarization is homogeneous, then spin diffusion will not cause any change in local polarization, and enhancement would be constant as a function of the polarization time.

For a system with a source and a large target, the normalized signal follows a multi (or stretched) exponential build-up:

$$S(t) = 1 - e^{-\left(\frac{t}{T_B}\right)^\beta} \quad (8)$$

where T_B is the effective build-up time with or without μwave irradiation. In the case of a homogeneous system, spin diffusion has no effect on local polarization, and the signal build-up will be mono exponential ($\beta = 1$). The build-up time of the signal build-up in μwave on ($T_{B,\text{ON}}$) and off ($T_{B,\text{OFF}}$) is then the same, and so the enhancement is constant.

As mentioned earlier, the difference between thin and thick border cases has an effect on enhancement at early times, and Figure 5b shows that this is predicted to lead to a completely different enhancement behavior. For the thin border case, the enhancement decreases monotonically as a function of time. The thick border case is significantly different with an increase in the enhancement at early times, followed by a decay.

The late stage decay of enhancement as a function of time can be explained physically as follows. With time, the target polarization builds up to 1 in the μwave off case (without considering depolarization), whereas it is far from reaching ϵ_0 in the μwave on case, because of longitudinal relaxation (see Figure 4b & 4d). Thus, with time, the target polarization increases relatively more in the μwave off than in the μwave on case. This explains the late stage decay of the enhancement seen in both thick and thin border cases. The early time increase in enhancement seen for the thick border case is rationalized by looking at the source behavior in the border region, as described in detail in SI.

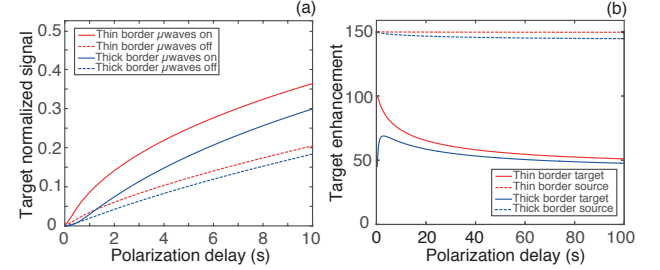


Figure 5. (a) Simulations of normalized target signal build-up as a function of time in absence and in presence of microwave irradiation for a thin border (red) and a thick border (blue). (b) Simulated enhancement as a function of time in the target (solid lines) and in the source (dashed lines) for a thin border (red) and a thick border (blue). In all simulations, $L = 2 \mu\text{m}$, $T_{B,\text{source}} = 100 \text{ ms}$, $T_{1,\text{target}} = 100 \text{ s}$, $\epsilon_0 = 150$, $D_{\text{target}} = D_{\text{source}} = 1.0 \cdot 10^{-3} \mu\text{m}^2 \text{ s}^{-1}$.

In summary, in Figure 5b we see that the nature of the border influences the behavior of the enhancement at early times, and that the decay to a steady state enhancement at later times in both cases is a universal signature of relayed spin diffusion.

We note in Figure 5a that the observable build-up time is always shorter for μwave on than off. This is easily explained by the fact that the gradient of polarization between the source and the target is much larger with than without DNP. We also note that $T_{B,\text{target}} < T_{1,\text{target}}$. This arises from the fact that spin diffusion, both in μwave on and off cases, connects polarization between the source and the target and since $T_{B,\text{source}}$ is here always shorter than $T_{1,\text{target}}$, this accelerates the effective build-up time in the target. Specifically, fitting the build-up curves of Figure 5a to a stretched exponential, we find that $T_{B,\text{target}}$ is always shorter than 42 s, whereas $T_{1,\text{target}} = 100 \text{ s}$. An important consequence of this observation is that, since proportionally more spins are closer to the source in smaller objects, we predict shorter build-up times for smaller objects. Figure 6 shows simulations of the normalized signal build-up curves and enhancements of the target for a spherically symmetric object, for different target sizes.

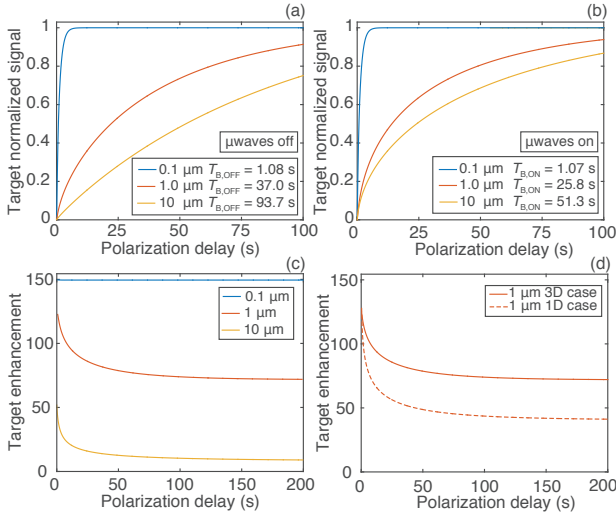


Figure 6. Spherical targets with a thin border. Simulations of normalized signal build-up curves for different target radii as a function of time for (a) μ waves off and (b) μ waves on. Build-up times T_B were determined from a fit to a stretched exponential. (c) Enhancement of the target as a function of time for different radii. (d) Enhancement of the target for a spherical and a linear geometry. In all simulations, $T_{B,source} = 100$ ms, $T_{1,target} = 100$ s, $\epsilon_0 = 150$, and $D_{target} = D_{source} = 1.0 \cdot 10^{-3} \mu\text{m}^2 \text{s}^{-1}$.

In Figure 6a & 6b, as expected, the build-up time of the target is predicted to increase with the size of the object. The enhancement decreases with the size of the target, since relaxation in the target destroys the propagating hyperpolarization before it has time to spin diffuse through the whole target, (Figure 6c). As shown in Figure 6d, we observe that the enhancement of a spherical object is higher, with all other parameters being identical, than the enhancement for a linear object being polarized from the ends. Indeed, with the same polarizing length L , the spherical symmetry offers less target volume to be polarized for unit of polarizing surface with respect to the linear symmetry. For a diffusion in 2 dimensions, we expect a curve in between the two shown.

Build-up Time and Steady State Enhancement Behavior.

As shown in Figure 6b, the build-up time depends on the size of the target, ranging from $T_{B,target} = T_{B,source} = 3$ s for an infinitely small target (which corresponds to a homogeneous system), and tends to $T_{1,target}$ for an infinitely large target. (The values of the β coefficient of the stretched exponentials are shown in Figure S15.)

At long polarization times, a steady state is achieved in which relaxation exactly balances diffusion polarization flow into the target. The change in the steady-state enhancement as a function of the size of the object is shown in Figure 7. The great interest of the steady state enhancement is that it does not depend on the nature of the border. As shown below, the steady state enhancement is only a function of the geometry (linear, cylindrical or spherical), the length L , the relaxation time $T_{1,target}$ and the diffusion rate D_{target} .

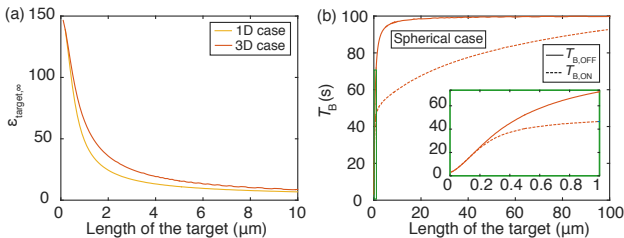


Figure 7. (a) Simulated enhancement of the target at steady state as a function of the size of the target for spherically and linearly symmetric objects with thin borders. (b) Simulated build-up times of the target as a function of the size of the target for a spherically symmetric object. In all simulations, $T_{B,source} = 3$ s, $T_{1,target} = 100$ s, $\epsilon_0 = 150$, and $D_{target} = D_{source} = 1.0 \cdot 10^{-3} \mu\text{m}^2 \text{s}^{-1}$.

We choose to fit the curves in Figure 7a with:

$$\epsilon_\infty = 1 + (a - 1) \frac{2\sqrt{b}}{L} \tanh\left(\frac{L}{2\sqrt{b}}\right) \quad (9a)$$

for the 1D case and

$$\epsilon_\infty = 1 + (a - 1) \frac{3\sqrt{b}}{L} \left[\coth\left(\frac{L}{\sqrt{b}}\right) - \frac{\sqrt{b}}{L} \right] \quad (9b)$$

for the 3D case where ϵ_∞ is the steady state enhancement of the target, a and b are fitting parameters, and D and T_1 are the diffusion rate and relaxation time in the target, respectively. The reasoning behind the choice of these functions is given in SI. By inspection, the fitted values of a and b are found to be

$$a = \epsilon_0 \quad (10)$$

where ϵ_0 corresponds to the enhancement of the source (which is constant) and

$$b = D \cdot T_1 \quad (11)$$

A phenomenological relation between the steady state enhancement and the size of the object can thus be determined as:

$$\epsilon_\infty = 1 + (\epsilon_0 - 1) \frac{2\sqrt{D \cdot T_1}}{L} \tanh\left(\frac{L}{2\sqrt{D \cdot T_1}}\right) \quad (12a)$$

for the 1D case and

$$\epsilon_\infty = 1 + (\epsilon_0 - 1) \frac{3\sqrt{D \cdot T_1}}{L} \left[\coth\left(\frac{L}{\sqrt{D \cdot T_1}}\right) - \frac{\sqrt{D \cdot T_1}}{L} \right] \quad (12b)$$

for the 3D case. Similar fitting was done for the cylindrical (or 2D) case, leading to a steady state enhancement of:

$$\epsilon_\infty = 1 + (\epsilon_0 - 1) \frac{2\sqrt{D \cdot T_1}}{L} \left[\frac{I_1\left(\frac{L}{\sqrt{D T_1}}\right)}{I_0\left(\frac{L}{\sqrt{D T_1}}\right)} \right] \quad (12c)$$

where I_0 and I_1 are the zero and first order modified Bessel functions, respectively.

We can reinforce this observation by noting how the diffusion equation (1) behaves at steady state. In the absence of depolarization, without microwave irradiation, $P_{0,off} = 1$ in the target. With microwave irradiation, we also have $P_{0,on} = 1$ in the target. Then, assuming that the diffusion and relaxation times are constant in the target (which is reasonable, e.g., for a border thickness of 2 nm), for one-dimensional spin diffusion, the steady state solution in the target is:

$$P(x, \infty) = A e^{\frac{x}{\sqrt{D T_1}}} + B e^{-\frac{x}{\sqrt{D T_1}}} + 1 \quad (13)$$

where A and B depend on the boundary conditions (see details in SI). This is in agreement with previous results.^{14,58} We observe that the position dependence is scaled by the term $\sqrt{D T_1}$, and the polarization is in fact a function of the characteristic diffusion length $\rho = \frac{x}{\sqrt{D T_1}}$ as detailed in the SI. This observation rationalizes the phenomenological form of b observed for the steady state enhancement in equations 12.

Experimental Results.

To support the predictions made above we have performed experiments on three prototypical systems.

Homogeneous sample.

The homogeneous case was verified with a sample of histidine dissolved in glycerol- d_8 :D₂O:H₂O (60:30:10) with AMUPol as the biradical polarization source²¹ and recording the enhancement of the signals from histidine and glycerol. The prediction is that a homogeneous system displays a constant enhancement as a function of polarization time. As shown in Figure 8a, the histidine ¹³C NMR peaks are much broader than the peaks observed when the crystalline histidine is impregnated with a radical solution remotely polarized (see Figure 10a). The signal build-up of histidine peaks was recorded with a CP saturation-recovery experiment. The μ waves on build-up time was the same as the solvent build-up time as shown in Figure 8b, confirming that the histidine, glycerol, water, and radical molecules are homogeneously mixed. As shown in Figure 8c, the enhancement of both histidine and glycerol was found to be constant over 15 s, which confirms the prediction. The measurement error is relatively large for the histidine peaks since the signal to noise ratio was poor in the μ waves off spectra even with 2048 scans (8.5 hours), due to low concentration of histidine.

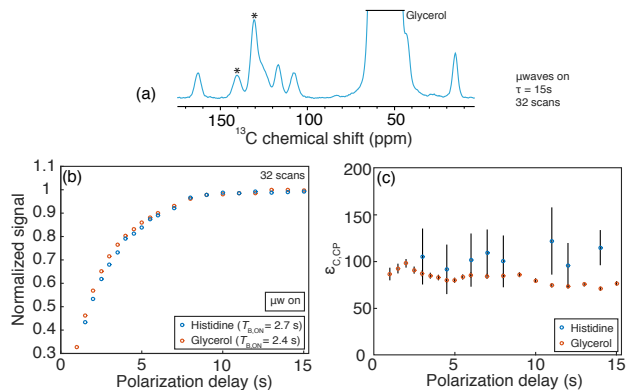


Figure 8. (a) ¹³C CPMAS DNP enhanced solid-state NMR spectrum of histidine with microwave irradiation obtained at 105 K, 8 kHz MAS, and $B_0 = 9.4$ T. For spectrum (a), around 0.5 mg of powdered histidine was dissolved in 100 μ L of glycerol- d_8 :D₂O:H₂O (60:30:10) containing 12 mM AMUPol. The polarization delay was set to 15 s. (b) Normalized signal build-up with microwave irradiation of the histidine and glycerol peak areas as a function of the polarization delay and (c) the corresponding enhancement of the histidine and glycerol signals. The asterisks indicate spinning sidebands.

Heterogeneous samples: microcrystalline powder

To confirm predictions of the simulations that signal build-up times depend on the size of the target in heterogeneous samples, ¹³C detected ¹H build-up times of histidine signals were measured when the histidine was either dissolved in a radical containing solution, ground then impregnated with a solution, unground and impregnated, and for the dry powder alone. As shown in Figure 9, the build-up time clearly increases with the size of the particle, ranging for the μ waves on case from 2.7 s for the homogeneous solution to 435 s when the size of the particles is large, up to 1038 s for the dry powder which corresponds to the intrinsic T_1 of crystalline histidine. As predicted for heterogeneous systems shorter build-up times are measured for μ waves on than for μ wave off for the impregnated powders.

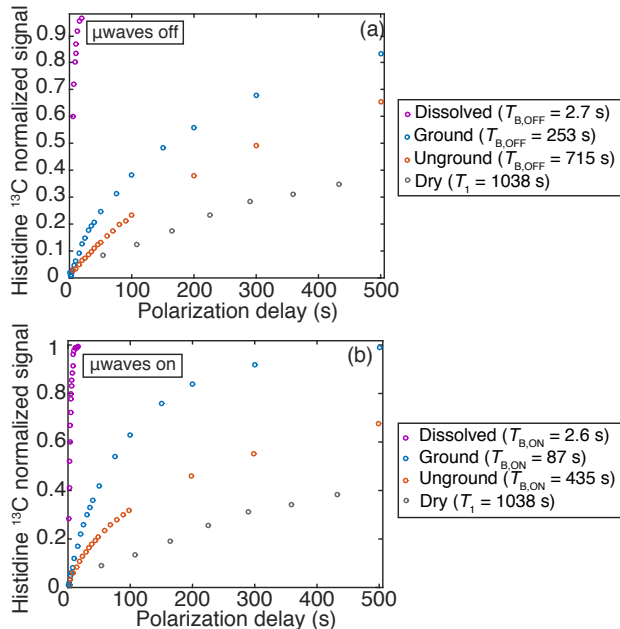


Figure 9. Signal ¹H build-up curves detected through the signal of the ¹³C peaks in CPMAS NMR spectra recorded at 105 K, 8 kHz MAS, and $B_0 = 9.4$ T (a) without and (b) with microwave irradiation of either dry, ground, unground or dissolved powders of histidine hydrochloride monohydrate. The dissolved sample was in glycerol- d_8 :D₂O:H₂O (60:30:10) with 12 mM AMUPol. The impregnation was done with 1,1,2,2-tetrachloroethane (TCE) containing 16 mM of TEKPol. All signals were normalized using the steady state value from the exponential fits.

Figure 10a shows the DNP enhanced spectrum from a sample of microcrystalline histidine ground for five minutes to reduce particle sizes and impregnated with 1,1,2,2-tetrachloroethane (TCE) containing 16 mM of the TEKPol biradical.²⁰ We notice that the histidine ¹³C NMR peaks are much narrower in this heterogeneous sample than in the homogeneous solution of Figure 8, since the organic domains now remain crystalline. In Figure 10b we show the normalized signal build-up of TCE as a function of the polarization delay with and without microwave irradiation, together with the prediction for the homogenous solvent. Simulations are overlaid on the experimental data points. Analogously to the homogeneous case, the build-up time does not depend on the μ wave irradiations since the TCE domains contain homogeneously dispersed radicals. The enhancement of the TCE signal is thus found to be constant, as shown in Figure 10c. The build-up of the histidine peaks with and without microwave irradiation is shown in Figure 10d, together with the prediction for spherical domains of radius of 2.3 μ m (see figure caption for the other parameters), which is in good agreement with the size measured in SEM images (see SI). The same system was also studied by DNP with unground particles as shown in SI and a 9 μ m average particle radius was determined.

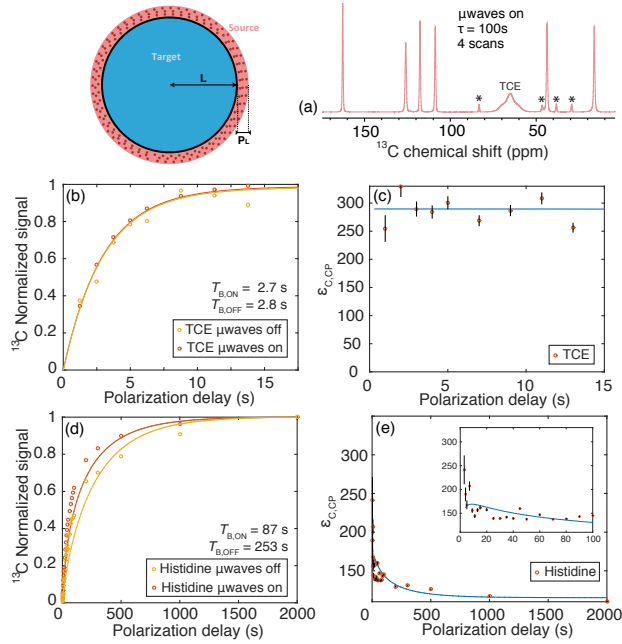


Figure 10. (a) ^{13}C CPMAS DNP enhanced solid-state NMR spectra obtained at 105 K, $B_0 = 9.4$ T and 8 kHz MAS of microcrystalline histidine which was ground by hand for 5 minutes and impregnated with a solution of TCE containing TEKPol. (b) ^{13}C CPMAS normalized signal build-up of the TCE peaks with and without microwave irradiation. Normalization was performed using the value of the signals at steady from a stretched exponential fit. (c) ^{13}C CP DNP enhancement of TCE peaks as a function of the polarization delay. (d) Signal build-up of histidine peaks with and without microwave irradiation as a function of the polarization delay. (e) ^{13}C CP DNP enhancement of histidine peaks as a function of the polarization delay. The histidine build-up points correspond to the average of the integrated areas of all the histidine ^{13}C peaks. Error bars were calculated by propagation of error using the noise levels of the spectra acquired with and without microwave irradiation as the standard deviation. In Figures (d) and (e) numerical simulations are overlapped for particle with spherical symmetry with: $L = 2.3 \mu\text{m}$, $T_{B,\text{source}} = 2.7$ s, $T_{1,\text{histidine}} = 1038$ s, $D_{\text{target}} = 1.10^{-3} \mu\text{m}^2\text{s}^{-1}$, $D_{\text{source}} = 1.3 \cdot 10^{-4} \mu\text{m}^2\text{s}^{-1}$, $P_L = 1 \mu\text{m}$, and $\epsilon_{\text{Depo}} = 0.5$. The asterisks indicate spinning sidebands.

Heterogenous samples: porous materials

A mesoporous material MatImPh-dTMS was impregnated with a TCE solution containing TEKPol²² as shown in Figure 11.

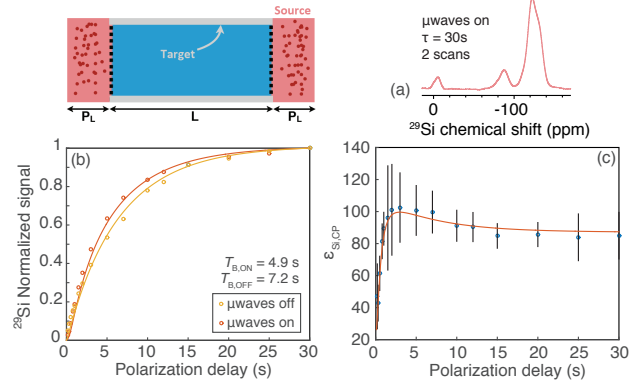


Figure 11. (a) ^{29}Si CPMAS DNP enhanced solid-state NMR spectra obtained at 105 K, $B_0 = 9.4$ T and 8 kHz MAS of the mesoporous material MatImPh-dTMS impregnated with TCE containing 16 mM of the biradical TEKPol²². (b) ^{29}Si CPMAS normalized signal build-up of the silicon peaks with and without irradiations. The signals were normalized to that of the longest polarization delay. (c) ^{29}Si CP

DNP Enhancement of the ^{29}Si signal as a function of the polarization delay. In Figures (c) and (d) numerical simulations are overlaid for one-dimensional diffusion with the following parameters: $L = 0.75 \mu\text{m}$, $T_{B,\text{source}} = 442$ ms, $T_{B,\text{TCE}} = 8$ s, and $D_{\text{target}} = D_{\text{source}} = 1.2 \cdot 10^{-4} \mu\text{m}^2\text{s}^{-1}$.

Here we assume that the bulky radical 22 cannot thoroughly enter the pore^{16,56,57} so that the silicon sites on the pore surface are polarized by spin diffusion through the solvent as illustrated in Figure 3. The enhancement behavior here is indeed found to be in extremely good agreement with the predictions of this model, including the details of the rising and then decaying enhancement for early polarization times, for a pore length of $0.75 \mu\text{m}$.

Heterogenous samples: polymer composites

EC/HPC coated microcrystalline cellulose (MCC) pellets were impregnated with 16 mM TOTAPOL biradical in glycerol- d_8 : D_2O : H_2O (60:30:10) solution as shown in Figure 12.

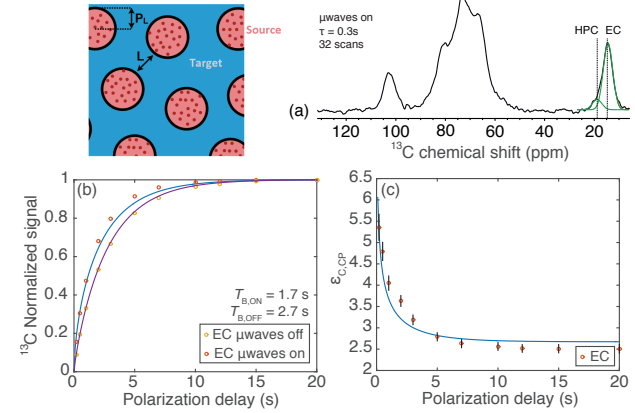


Figure 12. ^{13}C CPMAS DNP enhanced solid-state NMR spectra obtained at 105 K, $B_0 = 9.4$ T and 8 kHz MAS for EC/HPC coated MCC pellets with 16 mM TOTAPOL biradical in glycerol- d_8 : D_2O : H_2O (60:30:10) solution. Since the resolution of EC and HPC methyl peaks is only partial, deconvolution was used to obtain the peak intensities (illustrated in green). (b) ^{13}C CPMAS normalized signal build-ups of the EC peak. Normalization was performed using the value of the signals at steady state from a stretched exponential fit. (c) ^{13}C CP DNP enhancement of the EC peak as a function of the polarization delay. Error bars were calculated by propagation of error using the noise levels of the spectra acquired with and without microwave irradiation as the standard deviation. In Figures (c) and (d) numerical simulations are overlapped for one-dimensional diffusion with the following parameters: $L = 200$ nm, $T_{B,\text{source}} = 5$ ms, $T_{1,\text{target}} = 3.5$ s, $D_{\text{target}} = D_{\text{source}} = 2.10^{-4} \mu\text{m}^2\text{s}^{-1}$, $P_L = 42$ nm, and $\epsilon_{\text{Depo}} = 0.5$. The ratio of EC/HPC lengths was fixed to 70/30.

Here we assume that the aqueous polarization source impregnates the soluble HPC domains, but that it does not penetrate the insoluble EC domains, which are thus considered as the target. The enhancement behavior here is again found to be in extremely good agreement with the predictions of this model, including the details decaying enhancement for early polarization times, for EC domains of $0.2 \mu\text{m}$. This is in agreement with measurements made using NMR PRE type approaches.¹⁸

Heterogeneous samples: colloidal suspensions

Finally, insoluble EC Aquacoat nanoparticles were suspended in a solution of 16 mM bCTbK²⁰ in TCE/MeOH (80:20). The relayed DNP measurements shown in Figure 13 are in excellent agreement with a one-dimensional diffusion model with a diameter of 170 nm, which is in good agreement with the 169 nm average measured by dynamic light scattering.

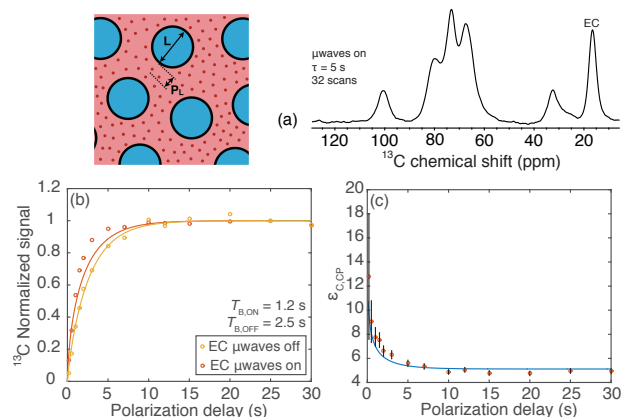


Figure 13. ^{13}C CPMAS DNP enhanced solid-state NMR spectra obtained at 95 K, $B_0 = 9.4$ T and 8 kHz MAS of EC nanoparticles impregnated with TCE/MeOH containing bCTbK. (b) ^{13}C CPMAS normalized signal build-up of the EC peak. Normalization was performed using the value of the signals at steady of a stretched exponential fit. (c) ^{13}C CP DNP enhancement of the EC peak as a function of the polarization delay. Error bars were calculated by propagation of error using the noise levels of the spectra acquired with and without microwave irradiation as the standard deviation. In Figures (c) and (d) is overlapped the numerical simulations of a linear system with the following parameters: $L = 170$ nm, $T_{B,\text{source}} = 5$ ms, $T_{1,\text{target}} = 3.7$ s, $P_L = 20$ nm, $D_{\text{target}} = D_{\text{source}} = 2.10^{-4} \mu\text{m}^2 \text{s}^{-1}$ and $\epsilon_{\text{Depo}} = 0.5$.

Size distributions and the correlation between size and the diffusion constant.

In the descriptions above we have assumed a single value of the particle sizes present in the samples. Of course, the same approach can be used to model the spin diffusion behavior in samples with particle size distributions by modeling the sums of the curves calculated above. For example, for the histidine crystals, a Weibull⁵⁹ distribution might be considered as was done by Rossini *et al.*^{15,17} This might produce better agreement in the early time behavior, though there is a clear danger of overfitting. For the case of the EC suspensions in Figure 13, no significant improvement is seen if a Weibull distribution is used to fit the data, as shown in SI. The only change is that the center of the distribution is slightly shifted (190 nm instead of 170 nm) due to the asymmetry of the Weibull distribution function.

Finally, we note that here that D is known to be typically between 0.2×10^{-3} and $1.0 \times 10^{-3} \mu\text{m}^2 \text{s}^{-1}$ in most organic solids.^{60,61} In the examples above we have assumed values of D most appropriate to each case on this basis, which allows us to deduce lengths from the build-up behaviors. As mentioned above, in cases where D cannot be measured experimentally independently, the result here is a measurement of the product $L \cdot D$.

Conclusions

We have shown how DNP NMR can be used in combination with models for polarization dynamics to determine the domain sizes in complex materials. This is achieved by measuring experimental polarization build-up curves in samples that are selectively doped with a radical containing source component. The observed polarization dynamics can be fully explained in terms of a simple model of spin diffusion between heterogeneous distributions of polarization within the sample. The DNP build-up times as well as the variation of the DNP enhancement as a function of the polarization time are found to be characteristic of the size and geometry of the micro- to nano-scale domains in the sample. We demonstrate the approach experimentally on four different systems where we successfully determine domain

sizes between 200 and 20 000 nanometers, specifically in powdered histidine hydrochloride monohydrate, the pore lengths of mesoporous silica materials, and domain sizes in two-component polymer film coatings. Additionally, we determine experimentally that even in the apparently homogeneous frozen solutions used as polarization sources in most DNP experiments, polarization is relayed from protons near the radicals to the bulk of the solution by spin diffusion, which confirms recent predictions⁴⁵ and explains the experimentally observed build-up times in these samples.

Supporting information

Additional materials and methods, additional simulations and the MATLAB code used here.

Acknowledgements

We are grateful to Matthew Conley and Christophe Copéret from ETH Zurich for providing the mesoporous silica materials. This work was supported by ERC Advanced Grant No. 320860. We are grateful to Prof. P. Tordo, Dr. O. Ouari and Dr. G. Casano (Aix-Marseille Université, France) for providing the biradicals used in the DNP NMR experiments.

References

- (1) Wilson, J. D.; Bechtel, D. B.; Todd, T. C.; Seib, P. A. Measurement of wheat starch granule size distribution using image analysis and laser diffraction technology *Cereal Chemistry* **2006**, *83*, 259-268.
- (2) Hendrich, C.; Favre, L.; Ievlev, D. N.; Dobrynin, A. N.; Bras, W.; Hormann, U.; Piscopiello, E.; Van Tendeloo, G.; Lievens, P.; Temst, K. Measurement of the size of embedded metal clusters by mass spectrometry, transmission electron microscopy, and small-angle X-ray scattering *Applied Physics a-Materials Science & Processing* **2007**, *86*, 533-538.
- (3) Amaral, S. S.; de Carvalho, J. A., Jr.; Martins Costa, M. A.; Pinheiro, C. An Overview of Particulate Matter Measurement Instruments *Atmosphere* **2015**, *6*, 1327-1345.
- (4) Clauss, J.; Schmidt-Rohr, K.; Spiess, H. W. Determination of Domain Sizes in Heterogeneous Polymer by Solid-State NMR *Acta Polymerica* **1993**, *44*, 1-17.
- (5) Demco, D. E.; Johansson, A.; Tegenfeldt, J. Proton spin diffusion for spatial heterogeneity and morphology investigations of polymers *Solid State Nucl. Magn. Reson.* **1995**, *4*, 13.
- (6) Schmidt-Rohr, K.; Spiess, H. W. *Multidimensional Solid-State NMR and Polymers*; Second ed.; Academic Press: London, 1996.
- (7) Graf, R.; Demco, D. E.; Gottwald, J.; Hafner, S.; Spiess, H. W. Dipolar couplings and internuclear distances by double-quantum nuclear magnetic resonance spectroscopy of solids *Journal of Chemical Physics* **1997**, *106*, 885-895.
- (8) Goldman, M.; Shen, L. Spin-Spin Relaxation in LaF3 *Phys. Rev.* **1966**, *144*, 321.
- (9) Schmidt-Rohr, K.; Clauss, J.; Blumich, B.; Spiess, H. W. Miscibility of polymer blends investigated by H-1 spin diffusion and C-13 NMR detection *Magnetic Resonance in Chemistry* **1990**, *28*, S3-S9.
- (10) VanderHart, D. L.; McFadden, G. B. Some perspectives on the interpretation of proton NMR spin diffusion data in terms of polymer morphologies *Solid State Nuclear Magnetic Resonance* **1996**, *7*, 45-66.
- (11) Schmidt-Rohr, K.; Clauss, J.; Blümich, B.; Spiess, H. W. Miscibility of polymer blends investigated by H-1 spin diffusion and C-13 NMR detection *Magn. Reson. Chem.* **1990**, *28*, S3.
- (12) Schmidt-Rohr, K.; Clauss, J.; Spiess, H. W. Correlation of structure, mobility, and morphological information in heterogeneous

polymer materials by 2-dimensional wideline-separation NMR spectroscopy *Macromolecules* **1992**, *25*, 3273-3277.

(13) Schlagnitweit, J.; Tang, M.; Baiaş, M.; Richardson, S.; Schantz, S.; Emsley, L. A solid-state NMR method to determine domain sizes in multi-component polymer formulations *Journal of Magnetic Resonance* **2015**, *261*, 43-48.

(14) van der Wel, P. C. A.; Hu, K. N.; Lewandowski, J.; Griffin, R. G. Dynamic nuclear polarization of amyloidogenic peptide nanocrystals: GNNQQNY, a core segment of the yeast prion protein Sup35p *Journal of the American Chemical Society* **2006**, *128*, 10840-10846.

(15) Rossini, A. J.; Zagdoun, A.; Hegner, F. S.; Schwarzwälder, M.; Gajan, D.; Copéret, C.; Lesage, A.; Emsley, L. Dynamic Nuclear Polarization NMR Spectroscopy of Microcrystalline Solids *Journal of the American Chemical Society* **2012**, *134*, 16899-16908.

(16) Lafon, O.; Thankamony, A. S. L.; Kobayashi, T.; Carnevale, D.; Vitthum, V.; Slowing, I.; Kandel, K.; Vezin, H.; Amoureux, J. P.; Bodenhausen, G.; Pruski, M. Mesoporous Silica Nanoparticles Loaded with Surfactant: Low Temperature Magic Angle Spinning C-13 and Si-29 NMR Enhanced by Dynamic Nuclear Polarization *Journal of Physical Chemistry C* **2013**, *117*, 1375-1382.

(17) Rossini, A. J.; Widdifield, C. M.; Zagdoun, A.; Lelli, M.; Schwarzwälder, M.; Copéret, C.; Lesage, A.; Emsley, L. Dynamic Nuclear Polarization Enhanced NMR Spectroscopy for Pharmaceutical Formulations *Journal of the American Chemical Society* **2014**, *136*, 2324-2334.

(18) Schlagnitweit, J.; Tang, M.; Baiaş, M.; Richardson, S.; Schantz, S.; Emsley, L. Nanostructure of Materials Determined by Relayed Paramagnetic Relaxation Enhancement *Journal of the American Chemical Society* **2015**, *137*, 12482-12485.

(19) Rossini, A. J.; Zagdoun, A.; Lelli, M.; Lesage, A.; Copéret, C.; Emsley, L. Dynamic Nuclear Polarization Surface Enhanced NMR Spectroscopy *Accounts of Chemical Research* **2013**, *46*, 1942-1951.

(20) Zagdoun, A.; Casano, G.; Ouari, O.; Schwarzwälder, M.; Rossini, A. J.; Aussenac, F.; M., Y.; G., J.; Copéret, C.; Lesage, A.; Tordo, P.; Emsley, L. Large Molecular Weight Nitroxide Biradicals Providing Efficient Dynamic Nuclear Polarization at Temperatures up to 200 K *Journal of the American Chemical Society* **2013**, *135*, 12790-12797.

(21) Sauvee, C.; Rosay, M.; Casano, G.; Aussenac, F.; Weber, R. T.; Ouari, O.; Tordo, P. Highly Efficient, Water-Soluble Polarizing Agents for Dynamic Nuclear Polarization at High Frequency *Angewandte Chemie-International Edition* **2013**, *52*, 10858-10861.

(22) Kubicki, D. J.; Casano, G.; Schwarzwälder, M.; Abel, S.; Sauvee, C.; Ganesan, K.; Yulikov, M.; Rossini, A. J.; Jeschke, G.; Coperet, C.; Lesage, A.; Tordo, P.; Ouari, O.; Emsley, L. Rational design of dinitroxide biradicals for efficient cross-effect dynamic nuclear polarization *Chemical Science* **2016**, *7*, 550-558.

(23) Song, C. S.; Hu, K. N.; Joo, C. G.; Swager, T. M.; Griffin, R. G. TOTAPOL: A biradical polarizing agent for dynamic nuclear polarization experiments in aqueous media *Journal of the American Chemical Society* **2006**, *128*, 11385-11390.

(24) Peersen, O. B.; Wu, X. L.; Kustanovich, I.; Smith, S. O. Variable-Amplitude Cross-Polarization MAS NMR *J. Magn. Reson. Ser. A* **1993**, *104*, 334-339.

(25) Haze, O.; Corzilius, B.; Smith, A. A.; Griffin, R. G.; Swager, T. M. Water-Soluble Narrow-Line Radicals for Dynamic Nuclear Polarization *Journal of the American Chemical Society* **2012**, *134*, 14287-14290.

(26) Bloembergen, N. On the interaction of nuclear spins in a crystalline lattice *Physica* **1949**, *15*, 386-426.

(27) Pinon, A. C.; Rossini, A. J.; Widdifield, C. M.; Gajan, D.; Emsley, L. Polymorphs of Theophylline Characterized by DNP Enhanced Solid-State NMR *Molecular Pharmaceutics* **2015**, *12*, 4146-4153.

(28) Bertini, I.; Luchinat, C. NMR of paramagnetic substances *Coordination Chemistry Reviews* **1996**, *150*, 1-252.

(29) Blumberg, W. E. Nuclear Spin-Lattice Relaxation Caused by Paramagnetic Impurities* *Physical Review* **1960**, *119*, 79-84.

(30) Rorschach, H. E. Nuclear Relaxation in solids by diffusion to paramagnetic impurities *Physica* **1964**, *30*, 38-39.

(31) Tse, D.; Lowe, I. J. Nuclear spin-lattice relaxation in CaF₂ crystals via paramagnetic centers *Physical Review* **1968**, *166*, 292-8.

(32) Brownstein, K. R.; Tarr, C. E. *Phys. Rev. A: At., Mol., Opt. Phys.* **1979**, *19*, 2446.

(33) Allen, S. G.; Stephenson, P. C. L.; Strange, J. H. Morphology of porous media studied by nuclear magnetic resonance *J. Chem. Phys.* **1997**, *106*, 7802.

(34) Bertini, I.; Luchinat, C.; Parigi, G. *Solution NMR of Paramagnetic Molecules: Applications to metalloproteins and models*, 2001.

(35) Rabbani, S. R.; Mendonça, C.; Mamani, J. B.; Rodriguez, H. C. Analysis of nuclear relaxation in granular systems *Braz. J. Phys.* **2006**, *36*, 28.

(36) Pintacuda, G.; John, M.; Su, X. C.; Otting, G. NMR Structure Determination of Protein-Ligand Complexes by Lanthanide Labeling *Acc. Chem. Res.* **2007**, *40*, 206.

(37) Lubach, J. W.; Xu, D.; Segmüller, B. E.; Munson, E. J. Investigation of the effects of pharmaceutical processing upon solid-state NMR relaxation times and implications to solid-state formulation stability *J. Pharm. Sci.* **2007**, *96*, 777.

(38) Dupre, N.; Martin, J. F.; Guyomard, D.; Yamada, A.; Kanno, R. Detection of surface layers using ⁷Li MAS NMR *J. Mater. Chem.* **2008**, *18*, 4266.

(39) Henrichs, P. M.; Linder, M.; Hewitt, J. M. Dynamics of the C-13 spin-exchange process in solids - a theoretical and experimental study *Journal of Chemical Physics* **1986**, *85*, 7077-7086.

(40) Suter, D.; Ernst, R. R. Spin diffusion in resolved solid-state NMR spectra *Physical Review B* **1985**, *32*, 5608-5627.

(41) Halse, M. E.; Zagdoun, A.; Dumez, J.-N.; Emsley, L. Macroscopic nuclear spin diffusion constants of rotating polycrystalline solids from first-principles simulation *Journal of Magnetic Resonance* **2015**, *254*, 48-55.

(42) Dumez, J. N.; Halse, M. E.; Butler, M. C.; Emsley, L. A first-principles description of proton-driven spin diffusion *Physical Chemistry Chemical Physics* **2012**, *14*, 86-89.

(43) Karabanov, A.; Wisniewski, D.; Lesanovsky, I.; Koeckenberger, W. Dynamic Nuclear Polarization as Kinetically Constrained Diffusion *Physical Review Letters* **2015**, *115*.

(44) Kubo, A.; McDowell, C. A. Spectral spin diffusion in polycrystalline solids under magic angle spinning *Journal of the Chemical Society-Faraday Transactions I* **1988**, *84*, 3713-3730.

(45) Mentink-Vigier, F.; Vega, S.; De Paëpe, G. Fast and accurate MAS-DNP simulations of large spin ensembles *Physical Chemistry Chemical Physics* **2017**.

(46) Mentink-Vigier, F.; Paul, S.; Lee, D.; Feintuch, A.; Hediger, S.; Vega, S.; De Paëpe, G. Nuclear depolarization and absolute sensitivity in magic-angle spinning cross effect dynamic nuclear polarization *Physical Chemistry Chemical Physics* **2015**, *17*, 21824-21836.

(47) Thurber, K. R.; Tycko, R. Perturbation of nuclear spin polarizations in solid state NMR of nitroxide-doped samples by magic-angle spinning without microwaves *Journal of Chemical Physics* **2014**, *140*.

(48) Paul, A.; Laurila, T.; Vuorinen, V.; Divinski, S. V. *Thermodynamics, diffusion and the Kirkendall effect in solids*; Springer, 2014.

(49) Fick, A. Ueber diffusion *Annalen der Physik* **1855**, *170*, 59-86.

(50) Girifalco, L. A. *Statistical Mechanics of Solids* Oxford University Press **2000**.

- (51) Kubicki, D. J.; Rossini, A. J.; Pura, A.; Zagdoun, A.; Ouari, O.; Tordo, P.; Engelke, F.; Lesage, A.; Emsley, L. Amplifying Dynamic Nuclear Polarization of Frozen Solutions by Incorporating Dielectric Particles *Journal of the American Chemical Society* **2014**, *136*, 15711-15718.
- (52) Zagdoun, A.; Rossini, A. J.; Gajan, D.; Bourdolle, A.; Ouari, O.; Rosay, M.; Maas, W. E.; Tordo, P.; Lelli, M.; Emsley, L.; Lesage, A.; Copéret, C. Nonaqueous Solvents for DNP Spectroscopy *Chemical Communications* **2012**, *48*, 654-656.
- (53) Hu, K. N.; Yu, H. H.; Swager, T. M.; Griffin, R. G. Dynamic Nuclear Polarization with Biradicals *Journal of the American Chemical Society* **2004**, *126*, 10844-10845.
- (54) Lange, S.; Linden, A. H.; Akbey, U.; Franks, W. T.; Loening, N. M.; van Rossum, B.-J.; Oschkinat, H. The effect of biradical concentration on the performance of DNP-MAS-NMR *Journal of Magnetic Resonance* **2012**, *216*, 209-212.
- (55) Ji, X.; Bornet, A.; Vuichoud, B.; Milani, J.; Gajan, D.; Rossini, A. J.; Emsley, L.; Bodenhausen, G.; Jannin, S. Transportable hyperpolarized metabolites *Nature Communications* **2017**, *8*, 13975.
- (56) Rossini, A. J.; Zagdoun, A.; Lelli, M.; Canivet, J.; Aguado, S.; Ouari, O.; Tordo, P.; Rosay, M.; Maas, W. E.; Copéret, C.; Farrusseng, D.; Emsley, L.; Lesage, A. Dynamic Nuclear Polarization Enhanced Solid-State NMR Spectroscopy of Functionalized Metal-Organic Frameworks *Angewandte Chemie-International Edition* **2012**, *51*, 123-127.
- (57) Pump, E.; Viger-Gravel, J.; Abou-Hamad, E.; Samantaray, M. K.; Hamzaoui, B.; Gurinov, A.; Anjum, D. H.; Gajan, D.; Lesage, A.; Bendjeriou-Sedjerari, A.; Emsley, L.; Basset, J.-M. Reactive surface organometallic complexes observed using dynamic nuclear polarization surface enhanced NMR spectroscopy *Chemical Science* **2017**, *8*, 284-290.
- (58) Crank, J. *The mathematics of diffusion*; Oxford university press, 1979.
- (59) Weibull, W. A Statistical Distribution Function of Wide Applicability *Journal of Applied Mechanics* **1951**, *18*, 293-297.
- (60) Roos, M.; Micke, P.; Saalwachter, K.; Hempel, G. Moderate MAS enhances local H-1 spin exchange and spin diffusion *Journal of Magnetic Resonance* **2015**, *260*, 28-37.
- (61) Wilhelm, M.; Feng, H.; Tracht, U.; Spiess, H. W. 2D CP/MAS C-13 isotropic chemical shift correlation established by H-1 spin diffusion *Journal of Magnetic Resonance* **1998**, *134*, 255-260.